Journal of The Electrochemical Society, **154** (10) B1049-B1058 (2007)
0013-4651/2007/154(10)/B1049/10/$20.00 © The Electrochemical Society

Active Water Management for PEM Fuel Cells

Shawn Litster, Cullen R. Buie, Tibor Fabian, John K. Eaton, and Juan G. Santiago[z]

Department of Mechanical Engineering, Stanford University, Stanford, California 94305, USA

Proton exchange membrane (PEM) fuel cells require humidified gases to maintain proper membrane humidification, but this often results in a problematic accumulation of liquid water. Typically, excessive air flow rates and serpentine channel designs are used to mitigate flooding at the cost of system efficiency. In this paper, we present an active water management system that decouples water removal from oxidant delivery. The system uses a porous carbon flow field plate as an integrated wick that can passively redistribute water within the fuel cell. The system also employs an external electro-osmotic (EO) pump that actively removes excess water from the channels and gas diffusion layer. For a 25 cm^2 fuel cell with 23 parallel air channels, we demonstrate a 60% increase in maximum power density over a standard graphite plate with a low air stoichiometry of 1.3. EO pumping represents a negligible parasitic load, consuming typically less than 0.5% of the fuel cell power. Experimental and modeling results show that simple passive water transport through the porous carbon alone can prevent flooding at certain operating conditions and flow field dimensions. However, active water management with EO pumping facilitates robust operation with a high volumetric power density across all operating conditions.
 [DOI: 10.1149/1.2766650]

Manuscript submitted February 1, 2007; revised manuscript received June 3, 2007. Available electronically August 17, 2007.

Water management is a persistent challenge for polymer electrolyte membrane (PEM) fuel cells with perfluorosulfonic acid (PFSA) type membranes, such as Nafion (DuPont, Wilmington, DE), which require high water activity for suitable ionic conductivity. Humidification of reactant gases ensures proper humidification of the membrane. Consequently, much of the water produced by the oxygen reduction reaction at the cathode is generated in liquid form. Liquid water invades the pores of the catalyst layer and gas diffusion layer (GDL) and restricts diffusion of oxygen to the catalyst. The liquid water emerges from the GDL via capillary action,[1-5] accumulates in gas channels,[6-19] covers the GDL surface, increases the pressure differentials along flow field channels,[20] and creates flow maldistribution and instability in systems with multiple parallel channels.[15,21]

A common strategy to mitigate flooding is to employ serpentine channels (most commonly a small number of serpentine channels in parallel) for the cathode and to supply air flow rates large enough to force liquid water out of the system. These strategies act in concert as serpentine designs increase flow rate per channel, improving the advective removal of water droplets. Air is often supplied at a rate several times greater than that required by the reaction stoichiometry, increasing the oxygen partial pressure at the outlet.[7,22] The use of high flow rate and high pressure contributes to air delivery being one of the largest parasitic loads on fuel cells.[23,24] Miniaturization of forced air fuel cells exacerbates this parasitic load issue as the efficiency of miniaturized pumps and blowers is typically much lower than that of macroscale pumps.[25,26]

Parallel channels can reduce the pressure differential across the flow field by orders of magnitude compared to serpentine channels. A parallel channel design also simplifies flow field machining and can enable novel fabrication methods.[27,28] However, truly parallel channel architectures are typically impractical as they are prone to unacceptable nonuniformity in air streams and catastrophic flooding. For example, Nguyen[29] demonstrated that parallel channels flood to a much higher degree than an interdigitated flow field, resulting in a 50% reduction in maximum current density at air stoichiometric ratios in excess of 4.7. Liu et al.[15] also showed significantly lower performance with their parallel flow field vs their serpentine and interdigitated designs. Liu et al.[21] used an optically accessible fuel cell with parallel channels and differential pressure measurements to show that channel flooding is well correlated with pressure differential across the cathode channels. Typically, air stoichiometries greater than 4 are necessary to prevent parallel channel flooding.[27]

Flooding is often associated with high-current-density operation because of increased water production and electro-osmotic drag.[30] However, the neutron radiography measurements of Trabold et al.[9] demonstrate that the greatest accumulation of water in the fuel cell channels can occur at low current densities (0.1 A/cm^2) because of the low air flow rates. Using neutron imaging, Hickner et al.[31] demonstrated that flooding at high current densities is also somewhat mitigated by temperature increases due to internal heating; this increases saturation pressure and evaporation rates. Further, in situ and ex situ visualizations show that considerable flooding occurs in the GDL directly under the rib of the flow field irrespective of current density.[1,3,18]

Several passive water strategies employ additional components to mitigate flooding.[32-34] Ge et al.[32] fabricated a PEMFC with absorbent 0.32 mm thick strips of wick inserted into the flow field of their machined (solid) graphite plates. The wicks effectively redistributed water for internal humidification of dry gases. However, this is not an example of the use of wicks to mitigate flooding as the system and conditions they explored were apparently not prone to flooding. In this and a subsequent publication,[33] they showed that a wick-free version of their fuel cell evaluated as a control did not suffer from cathode flooding. More recently, Sugiura et al.[34] fabricated a composite flow field plate featuring a thin water-absorbing layer and waste channels for removing liquid water from the oxidant channels. Their design, however, did not offer improved power density due to a significant increase in the ohmic losses introduced by the new components.

Active water management strategies in which applied pressure differentials actively transport liquid water out of or into a fuel cell are now emerging. Early work by Watanabe et al.[35] presented a PEM fuel cell that actively managed the water content of the electrolyte by supplying pressurized water to wicks that were integrated into the membrane. Yi et al.[36] presented an active water management method being developed by UTC Fuel Cells. In the UTC design, the bipolar plate is porous and has internal water channels for cooling and water removal. An applied pressure differential between the gas and water streams drives liquid water from the air channels and into internal channels dedicated to water transport.

Our group recently published the development of an active water management system utilizing electro-osmotic (EO) pumps for redistributing and removing liquid water.[37] The 1.2 cm^2 fuel cell featured a simple, single straight channel. Transient and polarization data demonstrated that the active removal of water with EO pumping eliminates flooding with a low parasitic load ($\sim$10% of the fuel cell power). EO pumps use the electric double layer (EDL) that forms between solid surfaces and liquids. In the case of water pumping using porous glass EO pump structures, silanol groups on the surface of the glass spontaneously deprotonate, creating a negative surface charge and a net-positive layer of mobile ions with a generated

[z] E-mail: juan.santiago@stanford.edu

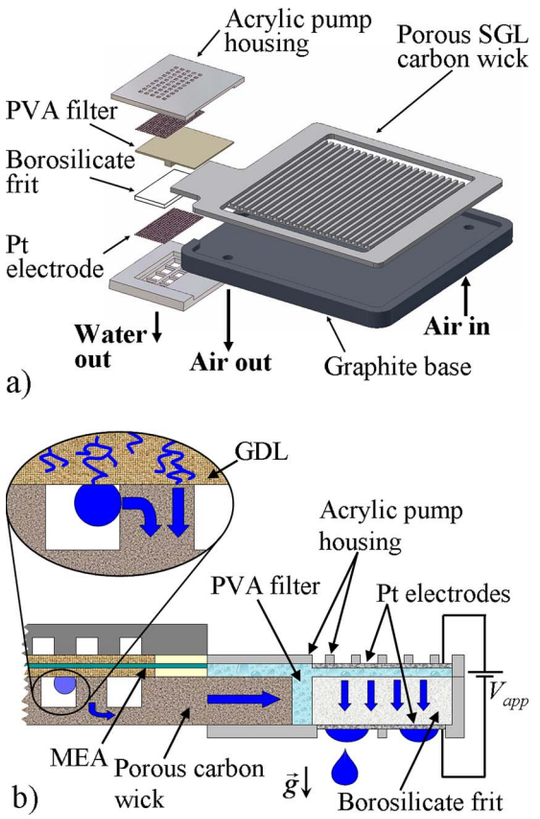

Figure 1. (Color online) Exploded assembly view of the 25 cm^2 fuel cell plate with a porous carbon wick and an external 2 cm^2 EO pump (a), and a schematic of the water pathway in an assembled wick and EO pump plate (b). The large, filled arrows indicate the flow of water.

potential of roughly −60 mV (a typical zeta potential for deionized water).[38] Applying electric potential across a porous glass substrate induces a Coulombic force on this mobile ion layer. The viscous interaction between ions and water generates a bulk flow. The working flow rate through an EO pump is a linear function of pressure load and the electric field imposed across the pump. A model for scaling of EO pumps with fuel cells is provided in Ref. 37. In general, EO pump flow rates scale linearly with area, an appropriate scaling for fuel cells whose output power and water production rate also scale with area. As we demonstrate in this paper, EO pumps also present a negligible parasitic load. References 38-40 provide further reading on EO pump theory and practical considerations.

In this paper, we present the incorporation of an EO pump into a larger 25 cm^2 PEM fuel cell with a new pump integration strategy. Unlike the cell of Ref. 37, in which EO pumps form the air channel structure, the current 25 cm^2 design has a small-area (2 cm^2) EO pump placed outside of the fuel cell hardware. This EO pump is hydraulically coupled to an internal wick structure. The porous carbon wick is an electrically conductive structure that simultaneously serves as current collector, a flow field/channel structure, and an actively controlled wick.

Experimental

Water management system.— Figure 1 illustrates our active water management system in which a hydrophilic porous flow field plate is hydraulically coupled to an external, relatively small area EO pump. Figure 1a shows an (approximately to scale) exploded schematic showing a solid graphite base, the porous carbon wick structure (also the current collector and channel wall substrate), and the EO pump assembly. The latter consists of a polyvinyl alcohol (PVA) filter which mates to a small tab machined into the wick (which protrudes from the stack structure), a porous borosilicate glass frit EO pump, platinum mesh electrodes, and a clam-shell design that holds the pump assembly together and allows water to escape. The function of these various components is depicted schematically in Fig. 1b. The hydrophilic porous carbon wick absorbs water droplets from the cathode channels and GDL, including water that normally accumulates under the rib of the flow field. Upon saturation with absorbed water, the wick can no longer remove water without application of a pressure gradient that pumps water out of the wick. This pumping action is accomplished by an external EO pump with only 8% of the area of the fuel cell. The EO pump and the wick are hydraulically coupled through a PVA filter which serves as both an easily compressed connector (a "bridge") between these components and a filter that keeps particles (e.g., carbon residue) from clogging the pump. Furthermore, the nonconductive PVA helps to electrically isolate the pump from the fuel cell. In this design, the EO pump is in close proximity to the air outlet; this location helps exploit air pressure gradients within the flow field in removing water from the wick.

The wick flow field is machined from porous carbon (SGL SIGRACET-plate PGP material, SGL Carbon AG, Germany). The 1.5 mm thick porous carbon plate is an untreated [e.g., without polytetrafluoroethylene (PTFE) or other materials] and nonwoven fibrous substrate similar to nonwoven GDL materials. As received from the manufacturer, the material does not spontaneously absorb water. We have experimented with various surface treatments and found that heat-treating the porous carbon transforms the surface into a hydrophilic state. For this study, we heat-treated the porous carbon in air at 300°C for 3 min (temperatures greater than 300°C result in measurable mass loss). The flow field has 23 channels which are 1.2 mm wide and 1 mm deep with 1 mm rib width. The header channel for the parallel flow field is 4.5 mm wide and 1.5 mm deep. A nonporous graphite base holds the porous carbon and provides gas sealing along most of the perimeter. A 2 cm wide section of the porous carbon protrudes 1 cm out of the graphite base as the connection to the EO pump.

The EO pump consists of a 2 cm^2 borosilicate frit (Robu-Glas, Germany) which is 1 mm thick and has an estimated mean pore diameter of 2 μm and 40% porosity (determined from dry/wet weight measurements). The electrodes are platinum mesh (Goodfellow Cambridge Limited, U.K.) with 0.06 mm diameter wires with center-to-center spacings of 0.25 mm. As received, the PVA material (PVA Unlimited, Warsaw, IN) has an uncompressed thickness of 2 mm and we sand it down to 1 mm thickness in the area covering the frit (to maximize electric field through the pump and reduce hydraulic resistance). As shown in Fig. 1a, the sanded horizontal tab of the PVA is sandwiched between the pump anode (pump inlet) and the frit; and the opposite horizontal tab is sandwiched between the acrylic housing and the porous carbon. The PVA is very hydrophilic[32] and has large pores (100–150 μm from optical measurements) for low hydraulic resistance. The PVA has an uncompressed porosity of 90% (from wet/dry measurements). The acrylic housing is composed of two laser-machined acrylic plates which compress both the pump assembly and the wick-to-PVA filter interface. The pump's anode plate has small $\sim 1 \times 1$ mm openings to allow the oxygen generated by electrolysis to escape, and the pump cathode plate has large openings for the pump's outlet. We seal the exposed perimeter of the frit by potting it into the acrylic housing with 5 Minute Epoxy (ITW Devcon, Danvers, MA).

Fuel cell hardware.— The fuel cell hardware is typical of 25 cm^2 single-layer fuel cells. The end plates are machined aluminum stock (McMaster-Carr, Los Angeles, CA) with four bolt-holes for compression. Both plates feature Kapton embedded heaters (McMaster-Carr) and K-type, sheathed thermocouples (Omega Engineering, Inc., Stamford, CT) in the centers of the plates. A 0.5 mm thick sheet of silicone rubber (McMaster-Carr) insulates the end plates from the current collector plates, which are copper plates

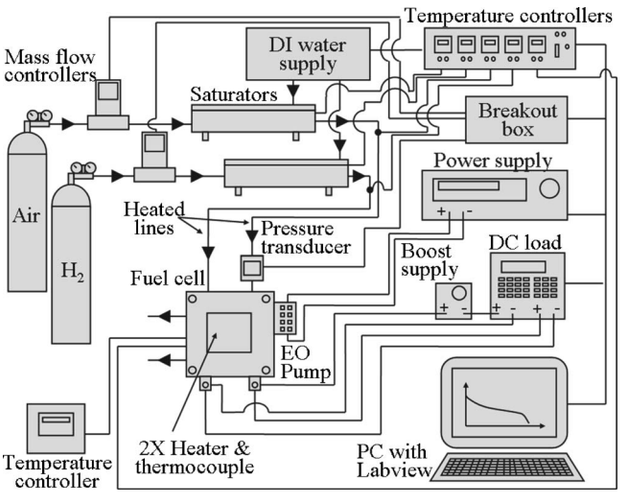

Figure 2. Schematic of the experimental setup. The system controls the air and hydrogen flow rates, temperature, and humidity. It also controls the fuel cell temperature and current, and the voltage applied to the EO pump. The system monitors the fuel cell's voltage, current, ohmic resistance, temperature, cathode pressure differential, and the EO pump current.

Table I. Experimental parameters.[a]

Parameter	Value
MEA	Ion Power CCM
Membrane thickness	25 μm
Platinum loading	0.3 mg Pt/cm^2
GDL	SGL SIGRACET 10-BB (nonwoven w/ MPL)
Fuel cell active area	25 cm^2
Anode gas	H_2 (>99.995%)
Anode outlet pressure	1 atm
Anode dew point	55°C
Hydrogen stoichiometry	2
Cathode gas	Air (extra dry)
Cathode outlet pressure	1 atm
Cathode dew point	55°C
Air stoichiometry (α)	1.5 unless otherwise noted
Endplate temperatures	55°C
Gas line temperatures	60°C
EO pump area	2 cm^2
EO pump voltage	12 V

[a] Where noted, a BCS MEA with a Nafion 111 membrane and carbon cloth GDLs is used in place of the Ion Power MEA.

(McMaster-Carr) with 1 μm thick layer of electroplated gold. A graphite plate (Fuelcellstore.com, Boulder, CO) with milled channels forms the anode's flow field plate. The anode flow field is a triple-serpentine with a channel width and depth of 0.75 mm and a rib width of 0.75 mm. As an experimental control and comparative study, we used a second cathode flow field; this was machined from nonporous graphite (Fuelcellstore.com) and has flow field dimensions identical to that of the porous carbon version of the cathode.

The membrane electrode assembly (MEA) consists of a catalyst-coated membrane from Ion Power, Inc., and nonwoven SGL SIGRACET 10-BB GDLs with microporous layers (Ion Power, Inc., Newcastle, DE). The membrane has a nominal thickness of 25 μm, and the catalyst layers have a total platinum loading of 0.3 mg Pt cm^{-2}. A 350 μm thick PTFE gasket (McMaster-Carr) surrounds the GDL and seals the gases. Bolt torques of 4.0 N m provide the assembly compression with the porous plate, and 2.8 N m was used for the assembly with a solid graphite cathode plate. Where noted, a MEA featuring a Nafion 111 membrane, a 1.0 mg Pt/cm^2 platinum loading, and carbon cloth GDLs (BCS Fuel Cells, Inc., Bryan, TX) was used in place of the Ion Power MEA.

Experimental setup.— As shown in Fig. 2, the fuel cell connects to a four-wire dc load (Agilent N3100A, Palo Alto, CA) in series with a boost power supply (Acopian W3.3MT65, Easton, PA). A dew-point control system (Bekktech LLC, Loveland, CO) conditions the gases to the desired dew point and temperature. The system also controls the temperature of both fuel cell end plates and the heated lines (Clayborn Labs, Inc., Truckee, CA) between the saturators and fuel cell. Mass flow controllers (Alicat Scientific, Tucson, AZ) regulate the flow of air and hydrogen from the gas cylinders. A dc power supply (Agilent 6030A DC Electronic Load) powers the EO pump at a constant voltage. A pressure transducer (PX139-030, Omega Engineering Inc.) measures the air pressure differential across the cathode flow field and manifolds. A PC featuring LabView software, a GPIB card, and IO data acquisition card (National Instruments, Austin, TX) controls system set points and records measurements.

To quantify the fuel cell's ohmic resistance, we developed a custom current interrupt method[41-43] employing the Agilent N3100A dc load and LabView software. During the resistance measurement, the dc load transiently pulses the fuel cell current between the set point and zero current. The transient pulse frequency is 120 Hz and the duty cycle of the zero current condition is 5%, which results in a zero current duration of 417 μs. During the transient pulsing, the Agilent load records the fuel cell voltage at a frequency of 100 kHz (10 μs/sample), the maximum sampling frequency of the load. LabView detects a single interrupt point and captures the transient voltage rise. We correct for initial impedance "ringing" by fitting the 20 data points from 100 to 300 μs after the interrupt with a straight line and extrapolating from this fit the value of the voltage rise immediately after the interrupt (0 μs).[43] We validated the interrupt and sampling methods by simultaneously monitoring the fuel cell voltage at 2.5 MHz with a digital oscilloscope (Agilent Infinium oscilloscope).

Table I lists the experimental parameters for the current studies. In all cases, we operate with gas dew points equal to the endplate temperatures. We use near-ambient pressure and set the endplate temperatures to 55°C, as this offers a reasonably efficient operating condition that is highly prone to flooding in the absence of active water removal. In preliminary experiments we also found that 55°C provides the highest power density provided there is no flooding. This near-optimum temperature condition is consistent with the experiments of Zaffou et al.,[44] who used UTC Fuel Cells' (South Windsor, CT) water transport plates and observed optimal performance at 60°C when using symmetric endplate temperatures and near-ambient pressure.

We initially conditioned the MEAs with voltage cycling between 0.3, 0.6, and 0.8 V (each for 20 s) over an 8 h period. Prior to acquiring measurements, we ran the fuel cell for 90 min using the same conditioning routine. Before each EO pump experiment, we removed the pump from the fuel cell and rinsed its components in deionized (DI) water to ensure repeatability.

Results and Discussion

The following transient and polarization results demonstrate that an EO pump coupled to a porous carbon flow field can dramatically enhance the performance of a larger 25 cm^2 PEM fuel cell while imposing a negligible parasitic load. The results include comparisons of three system configurations. These are the nonporous flow field and the porous carbon flow field, the latter with the EO pump off and on. As part of our study of these cases, we identify a non-negligible passive water management mechanism wherein at least some water is pumped through the wick by air pressure gradients alone. In the final section, we elaborate on this passive water transport mechanism and present a model of the flow in the wick. The

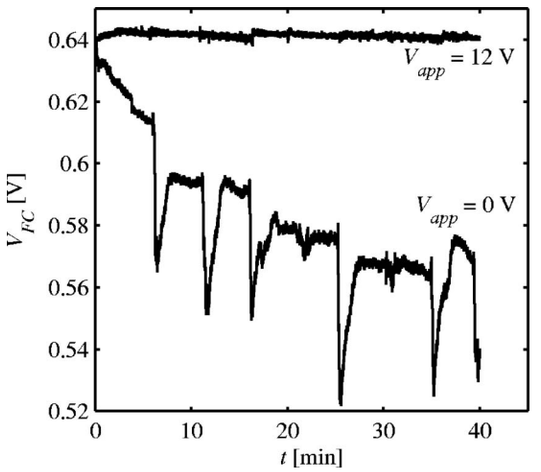

Figure 3. Transient fuel cell voltage at 0.5 A/cm^2 with the EO pump on and off. The applied voltage when the EO pump on is 12 V. The EO pump consumes 0.3% of the fuel cell power. The air stoichiometry is 1.5.

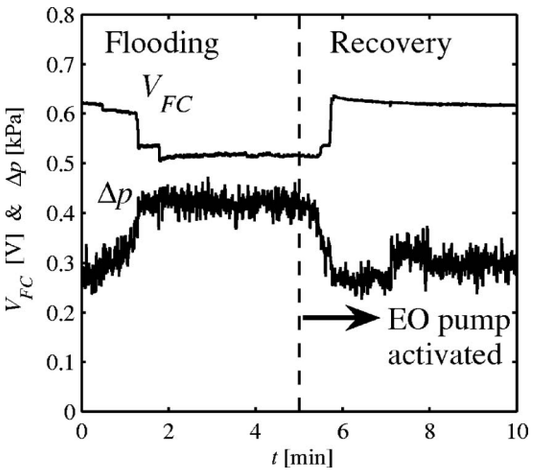

Figure 4. Fuel cell voltage (top curve) and air pressure differential (lower curve) during flooding and the recovery upon activating of the EO pump at t = 5 min and V_{app} = 12 V. The fuel cell current density was 0.5 A/cm^2 and α = 1.5. The BCS MEA with carbon cloth GDLs was used to obtain this result. Upon activation of the EO pump at an applied voltage of 12 V, the fuel cell recovers from the flooded cell value of 0.51 V to its original value of 0.62 V.

model and experimental results outline the inherent limitations of using a wick as a solely passive water management method.

Transient performance.— We first present individual-run, anecdotal data typical of the system and then proceed to averaged global quantification of performance such as polarization curves and average power. Figure 3 presents typical transient galvanostatic measurements of the fuel cell voltage for two conditions, one with the EO pump activated with an applied pump potential (V_{app}) of 12 V and the second with no applied voltage. We filter the transient data by convolving the digital time series with a Gaussian kernel that has a standard deviation of 250 ms, which is the average residence time of air in the flow field. Prior to each measurement, after the initial 90 min start-up, the fuel cell is run at the specified condition of j = 0.5 A/cm^2 and an air stoichiometry (α) of 1.5 for 10 min. The channels are then cleared by a gas purge (2000 sccm for 5 s). This procedure provides consistent initial conditions. When the EO pump is inactive, the fuel cell rapidly floods and exhibits strong voltage fluctuation and decay. The mean fuel cell voltage after 40 min, for four realizations with V_{app} = 0 V (to the pump), was 0.58 V. When the EO pump is activated at V_{app} = 12 V, the fuel cell voltage remains stable at the initial post-purge value of 0.64 V. We found the same result for applied pump potentials ranging from 5 to 40 V. Thus, after 40 min of operation the EO pump affords an average 10% increase in fuel cell power (23% at t = 25 min), while consuming 0.3% of the fuel cell power (P_{EO}/P_{FC} = 0.003). In addition, the EO pump greatly improves the transient stability of the fuel cell voltage.

Typical results such as those in Fig. 4 further elaborate the transient performance of the EO-pumped-wick fuel cell system. Here we show a case where the EO pump is at first deactivated for 5 min (resulting in flooding) and then activated. The figure shows typical time series of (the simultaneously measured) fuel cell voltage and air pressure differential (Δp) across the cathode flow field and manifolds. The fuel cell severely floods during the first 2 min of operation at 0.5 A/cm^2 and α = 1.5 and loses approximately 100 mV of the initial fuel cell voltage. Concurrently, the pressure differential increases by 50% due to the accumulation of liquid water in the channels. This is consistent with the work of Ref. 15 and 21. During this flooding, the voltage drops in sharp increments. As suggested by the visualization work of Yang et al.,[45] we hypothesize that these steps in voltage decrease are associated with water completely blocking air flow in a discrete number channels.

Upon activation of the EO pump at t = 5 min and V_{app} = 12 V, the fuel cell voltage recovers to the initial level within 40 s. The recovery represents a typical 20% increase in the fuel cell power relative to the partially flooded state. Similarly, the pressure differential sharply decreases with activation of the EO pump. Such transient recovery of the fuel cell voltage and decrease in pressure differential shows the ability of the EO pump to remove water from the cathode channels and recover from flooded conditions. He et al.'s[46] simultaneous measurements of current density and pressure drop demonstrated that doubling air flow rate can also remove liquid water and recover fuel cell performance. However, their 1.1 cm^2 fuel cell with interdigitated channels required more than 10 min at the higher air flow rate (and an approximately fourfold increase in air pumping power) for a full recovery.

Polarization curves.— This section presents polarization curves for three configurations of the 25 cm^2 fuel cell's cathode flow field: (*i*) a solid graphite plate, (*ii*) a porous carbon plate with no EO pumping, and (*iii*) a porous carbon plate with EO pumping (V_{app} = 12 V). For each configuration, we measure polarization curves for air stoichiometries (α) ranging from 1.3 to 6. An air stoichiometry of 1.3 is significantly lower than the typical values of 2-3 used for serpentine channels[15,37,47,48] and 4-5 for parallel channels.[27] Prior to the current work, a significantly higher air stoichiometry was typically necessary for fuel cells with parallel channel flow fields because of multichannel flow instabilities caused by liquid water accumulation.

We generated polarization curves by incrementing the current density by 0.1 A/cm^2 every 10 min. In this section, each measurement is a 2 min average taken at the end of a 10 min dwell period. We held open-circuit voltages (j = 0 A/cm^2) for 1 min and the measurement is the average of the last 30 s. Prior to acquiring these polarization curves, we ran the fuel cell at 0.8 A/cm^2 for 10 min to achieve consistent hydration and then purged the channels with high gas flow rates. We terminated the polarization curve measurements when the (instantaneous) fuel cell voltage fell below 0.2 V.

Figure 5a shows polarization curves for the fuel cell with a solid graphite flow field plate. We attribute the slight fluctuations in the high-current-density data to flooding (flooding is corroborated by noise in the voltage time series). At the lowest air stoichiometry (α = 1.3), a current density greater than 0.5 A/cm^2 cannot be achieved without the fuel cell voltage falling below 0.2 V due to severe flooding. The effects of flooding are apparent even with the

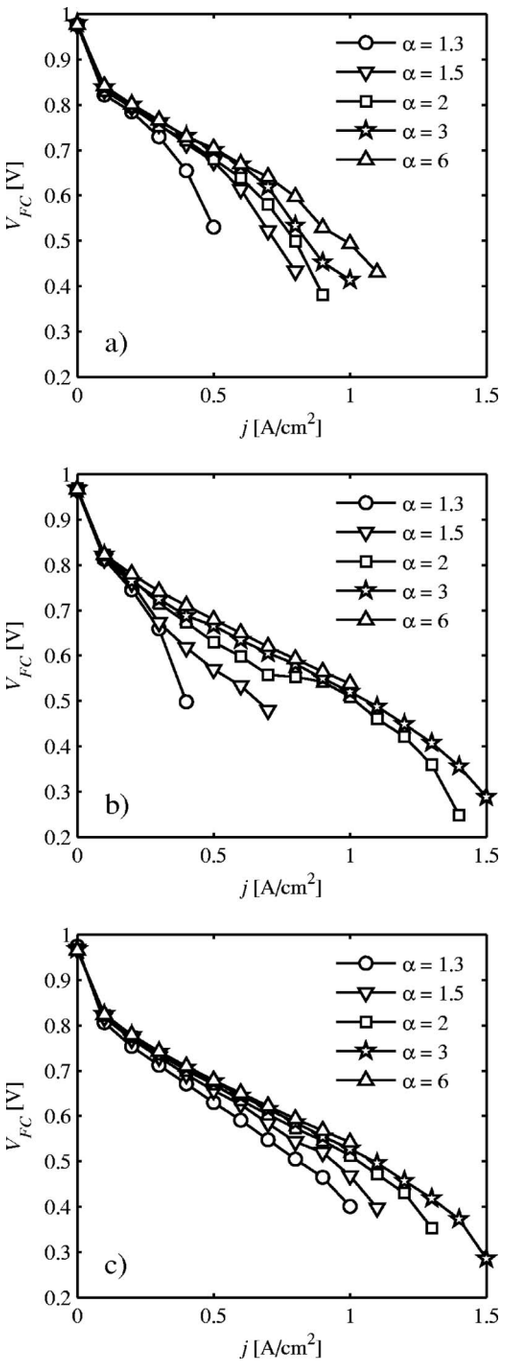

Figure 5. Polarization curves for the (a) solid graphite plate (cathode), (b) porous carbon plate (cathode) with the EO pump off, and (c) porous carbon plate with the EO pump activated at 12 V. Each set of polarization curves is shown for $\alpha = 1.3$–6. The solid graphite plate has the same flow field pattern and dimensions as the porous carbon plate. Each galvanostatic measurement is a time average of the last 2 min of a 10 min dwell period. Test conditions: fuel cell temperature 55°C, saturator temperatures 55/55°C (cathode/anode), outlet pressures 1/1 atm (cathode/anode).

highest air stoichiometry ($\alpha = 6$) at current densities greater than about 0.8 A/cm^2. The solid graphite flow field plate therefore requires very high airflow rates ($\alpha > 6$) to mitigate flooding, an unfavorable and perhaps restrictive feature from the perspective of overall system efficiency. This poor performance due to flooding motivates the development of water management methods that enable parallel flow fields.

Figure 5b shows the polarization curves we obtained when using the porous carbon flow field with no EO pumping. We assembled the porous carbon version of the fuel cell with a previously uncompressed wick and a new MEA. The curves show a significant improvement in the maximum current density for $\alpha \geqslant 2$. However, there is significant flooding at low current densities for $\alpha \leqslant 2$ and for low air stoichiometry ($\alpha = 1.3, 1.5$). (We terminated the $\alpha = 6$ polarization curve at 1 A/cm^2 due to the maximum airflow rate limit of our test station.) The flooding at low current density is consistent with the neutron imaging by Trabold et al.,[9] who found that the greatest accumulation of water occurs at low current densities, such as 0.1 A/cm^2 in their fuel cell (again, presumably due to the limited effect of air stream convection on water droplets at low air flow rates).

Figure 5c presents the polarization curves when the EO pump is operating with an applied voltage of 12 V. This applied voltage provides robust operation across the entire spectrum of air stoichiometry and current density. The air stoichiometry has significantly less impact on polarization curves because flooding is no longer a factor. The most dramatic improvement is observed for $\alpha = 1.3$, in which the maximum current density is 2 and 2.5 times greater than that observed for the solid graphite plate and the porous carbon plate, respectively. The associated maximum power density at $\alpha = 1.3$ is now 0.43 W/cm^2, vs 0.27 and 0.2 W/cm^2, respectively, for the solid graphite plate and the porous carbon with no EO pumping.

IR-free comparisons.— Use of a porous carbon flow field structure introduces an additional ohmic resistance to the system that slightly lowers its performance. To quantify this, we here analyze ohmic-resistance-free polarization data. For each point in the polarization curves in Fig. 5, we measured the total resistance of the fuel cell every 10 s using our current interrupt scheme. The first plot in Fig. 6 shows fuel cell area-specific resistance, R_{FC}, for each polarization point. All R_{FC} values are largely independent of current density, showing proper PEM hydration for all cases. More importantly, the resistance of the solid graphite plate (denoted by SG) is an average of 0.10 Ω cm^2, compared to the 0.17 Ω cm^2 value for the porous carbon plate systems (with EO pump on or off). The $\sim$0.07 Ω cm^2 increase in resistance is the sum of the additional contact resistance and the lower conductivity of the porous material. The 25 μm thick Nafion membrane accounts for 0.05 Ω cm^2 of the resistance when fully humidified,[49] so the porous carbon assembly has $\sim$2.5 times the electrical resistance of the fuel cell with a solid graphite plate.

With R_{FC} measurements we can generate polarization curves that are free of the ohmic voltage loss (IR-free polarization curves). These polarization curves allow us to directly compare the impact of flooding (vs ohmic losses) on the three configurations because the IR-free voltage ($V_{FC}^{\text{IR-free}} \equiv V_{FC} + jR_{FC}$) is the sum of the activation and mass-transfer losses. Figure 6 presents the IR-free polarization curves for $\alpha = 1.3$–6 for each of the three configurations. The low-current-density overlap of the three configurations at $\alpha = 6$ establishes that the two Ion Power MEAs used for the porous carbon and solid graphite assemblies feature very similar kinetics and open-circuit voltages, as required for valid comparisons.

The IR-free polarization curves in Fig. 6 indicate stable performance for all air stoichiometries with the porous carbon plate with EO pumping. At $\alpha = 1.3$, the porous plate without EO pumping presents the most severe flooding. However, at $\alpha = 3$ and 6 the polarization curves for the porous plate without EO pumping are consistent with little or no flooding. This suggests that a fully saturated (with water) porous carbon wick can lead to severe flooding if there is no mechanism for water removal. Porous channel walls that are saturated with liquid may even increase the probability of channels being blocked by water (vs a dry wick or hydrophobic solid plate) as menisci offer numerous nucleation sites. We hypothesize

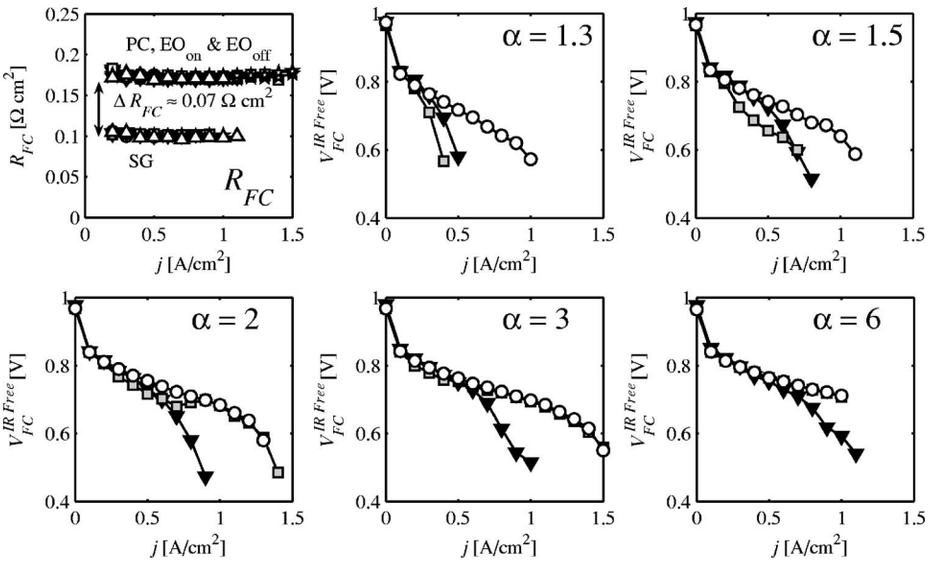

Figure 6. Area specific resistance measurements (R_{FC}) and IR-free polarization curves for α = 1.3–6. The polarization curves are for the porous carbon plate with an activated EO pump at V_{app} = 12 V (○), the porous carbon with the EO pump deactivated (□), and the solid graphite plate control case (▼). At α = 6, the polarization curves for the porous carbon with and without EO pumping have nearly identical values (data points overlap). Overall, implementation of a porous carbon plate adds an additional 0.07 Ω cm^2 of area specific resistance.

that the dramatic performance improvement with increased α is provided by a passive water removal mechanism through the wick. The high-air-pressure gradients at large values of α induce water transport through the porous carbon structure. In contrast to this situation, the IR-free fuel cell voltage of the solid graphite plate does not respond significantly to the same increases in air stoichiometry. This difference in response to air stoichiometry of the porous vs the solid plates supports a passive water removal mechanism via the porous carbon. We also hypothesize that low performance of the solid graphite plate at high current densities is partially due to water accumulation in the GDL under the flow field ribs, a region protected from flooding in the porous carbon setup.

Fuel cell power.— The following section quantifies the EO pump's effect on the net power generated by the fuel cell. Figure 7a presents the percent increase in fuel cell net power when the EO pump is activated vs the power generated by the fuel cell with the solid graphite plate

$$\chi \equiv \frac{P_{FC}^{EO,on} - P_{FC}^{SG}}{P_{FC}^{SG}} \quad [1]$$

Similar to the work of Buie et al.,[37] the percent increase in power with EO pumping is greater for lower air stoichiometries and higher current densities. EO pumping increases the fuel cell power by 10–44% at the maximum current densities achieved with the solid graphite configuration. At low current densities, the percent increase in power is slightly negative, as expected due to the increased ohmic resistance of the porous carbon and the parasitic load of the EO pump. Overall, the latter seems to us a small price to pay for strongly enhanced performance across a wide range of conditions. We also note that we here explore only cases where the EO pump is activated at full power at all operating conditions. We are currently exploring other pump control strategies (including feedback control).

Figure 7b shows the maximum power density of the three fuel cell configurations vs air stoichiometry. The data shows that EO pumping significantly increases maximum power density for operation at low air stoichiometries. At α = 1.3, the maximum power density with the EO pumping is 1.6 times greater than the case with the solid graphite plate. The maximum power density at this low stoichiometry is 2.1 times greater than that of the porous carbon with no EO pumping. Again, as shown in Fig. 6, the porous carbon with no EO pumping presents the most severe flooding at α = 1.3 and 1.5. However, for $\alpha \geq 2$ the porous carbon without EO pumping affords a higher maximum power density, which we attribute to

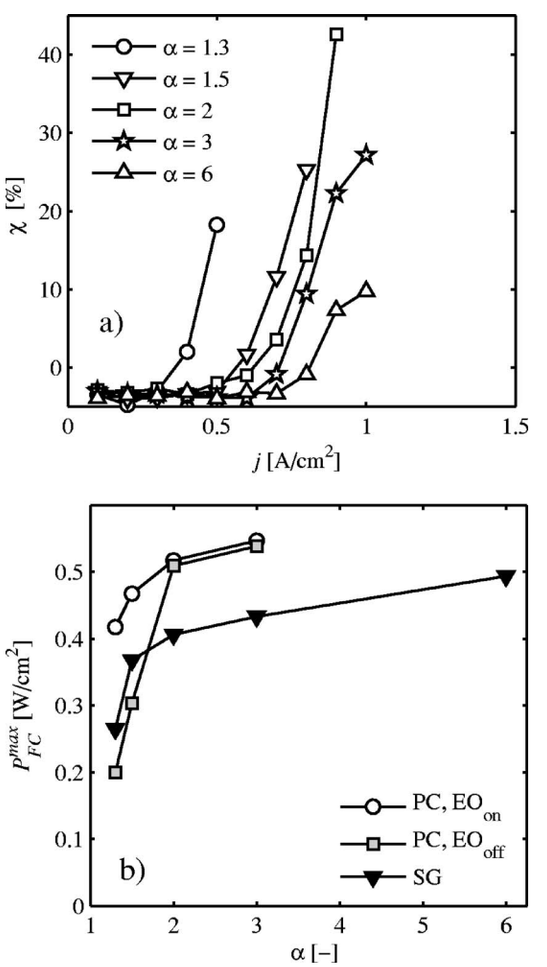

Figure 7. Percent increase in fuel cell power, χ, for the porous carbon plate with EO pumping vs the solid graphite plate (a), and the maximum fuel cell power vs air stoichiometry for the solid graphite plate (SG) and the porous carbon plate with EO pump on or off (PC,EO$_{on}$ and PC,EO$_{off}$, respectively) (b).

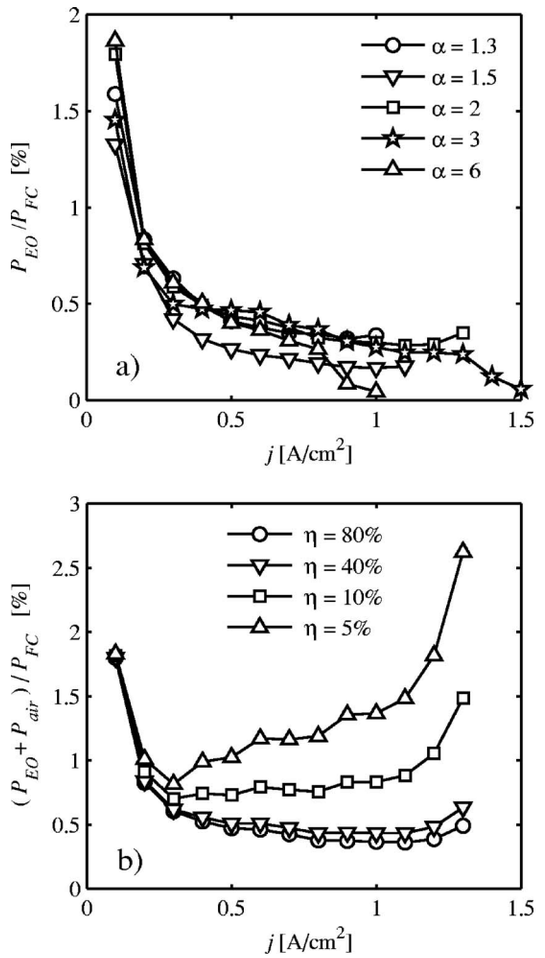

Figure 8. The parasitic load of the EO pump, P_{EO}/P_{FC}, (a) and the estimated total parasitic load, $(P_{EO} + P_{air})/P_{FC}$, (b) as a percentage of the fuel cell power vs current density. P_{EO} is relatively independent of fuel cell conditions (as long as the pump is saturated with water) and so the decrease in P_{EO}/P_{FC} at higher current densities is due mostly to increasing fuel cell power. The parasitic load of air delivery, P_{air}, is calculated with four assumed values of air pumping efficiency (η = 5, 10, 40, and 80%) for the polarization study with α = 2.

passive water removal. The plots also show that operating the solid graphite plate with a high stoichiometry (α = 6) does not provide the maximum power density of the EO-pumped porous carbon at a more efficient stoichiometry of α = 2.

EO pump parasitic power.— Figure 8a shows the measured power consumed by the EO pump for the polarization experiments of Fig. 5 and 6. We normalize the EO pump power as a fraction of the total electrical power generated by the fuel cell (P_{EO}/P_{FC}). For current densities greater than a low limit of 0.1 A/cm^2, the EO pump consumes less than 1% of the fuel cell power. The EO pump consumes less than 0.5% of the fuel cell power at moderate to high current densities (e.g., including the maximum power density conditions). Because flooding is avoided, there is little or no discernable effect of air stoichiometry on the relative EO pump power. One exception to this is for α = 3 and 6 and current densities greater than about 1 A/cm^2, where P_{EO}/P_{FC} drops sharply. We attribute this to the fact that at these high air flow rates, water removal from the system due to convection out of the cathode outlet becomes on the order of that pumped by the EO pump (thus, the void spaces between the EO pump's Pt mesh electrodes are not completely saturated with water and the pump consumes negligible power).

Relative to our original system described by Buie et al.,[37] the P_{EO}/P_{FC} power fraction is now more than an order of magnitude lower. One important reason for this is the significantly reduced pump area (relative to the fuel cell) used here (A_{EO}/A_{FC} here is now 0.08 vs 10 in our the previous work). In addition, the conductivity of the liquid water produced in our 25 cm^2 cell is significantly lower than that measured by Buie et al. The power for EO pumping is a strong function of water conductivity.[39] Our typical water conductivity is in the range of 8–10 μS/cm, vs the 170 μS/cm value for most of the measurements of Buie et al. They showed that this reduction of conductivity can be attributed to the elimination of iron-containing metals from the fuel cell hardware (see footnote 65 of Ref. 37). Iron ions react with the Nafion membrane and increases the fluoride emission rate, resulting in higher water conductivity.[50]

Figure 8b presents the total parasitic load expressed as the EO pump power plus the parasitic load of a theoretical air compressor or fan ($P_{air} = Q\Delta p/\eta$), where η is the thermodynamic efficiency of air pumping. Although air pumping delivery in macroscale devices can be quite efficient (η = 0.7 and higher), miniature fluid pumps have comparatively much lower efficiencies.[25] The relative parasitic load of air delivery, P_{air}/P_{FC}, for a fixed geometry flow field is highest near the maximum power condition as the air power scales as $P_{air} \propto \alpha^2 j^2$ (i.e., air power scales as $Q^2 R_h$, where R_h is hydraulic resistance). Because P_{EO}/P_{FC} scales as P_{FC}^{-1}, then $(P_{EO} + P_{air})/P_{FC}$ shows a strong parabolic minimum.

Note that the parasitic load of air delivery for this fuel cell is very low because of the parallel channel flow field. The modeling work of Shimpalee et al.[51] shows that the pressure differential, and thus the air delivery power, are roughly proportional to the inverse of number of channels squared ($P_{air} \propto 1/N^2$). So the pressure differential for a 26-channel design is about 33 times lower than that of a three-channel serpentine flow field.[51]

Flow field design and passive water management.— We have found that the porous carbon can effectively mitigate flooding in a passive manner, provided there is a sufficient pressure gradient in the air channels. As suggested by the data of Fig. 6, increasing air stoichiometry in the porous carbon plate device can significantly increase the performance. This is demonstratively not true of the solid graphite plate which flooded even at high air stoichiometry.

To further study the passive water management mechanism, we performed four additional polarization curves with a flow field featuring 33 0.75 × 0.75 mm parallel channels and a rib spacing of 0.75 mm. This flow field exhibits a greater hydraulic resistance because of the smaller hydraulic diameter of the channels. The measured pressure differential through the 33-parallel-channel flow field is approximately 5.3 times greater than that of the 23-parallel-channel design. Figure 9 presents polarization curves for this flow field with α = 1.5 and 2. Even at a low air stoichiometry of 1.5, there is no significant change in performance whether the EO pump was on or off with these channel dimensions.

We have attributed the dramatic performance improvement in the porous carbon flow field design (with the EO pump off) to air pressure gradients driving liquid water through the porous carbon toward the outlet. This mechanism occurs when channels are small or for high stoichiometries (because both yield large channel-to-ambient pressure differences). For simplicity, we here refer to this air-pressure-pumped flow of water through the wick as "passive" (although we understand that ultimately this action is provided by a small fraction of the power output of the air pump). We here propose a simple model that may in part explain these trends and compare its predictions to observations. Our model applies to highly hydrophilic wicks that are saturated with liquid water. For such systems, we postulate that water will preferentially travel through the hydrophilic wick in the upstream regions of the channel. Upstream, newly formed liquid water quickly enters the wick and is driven downstream. Further downstream, axial pressure gradients are insufficient to support all of the water flow through the wick. Beyond this point, we assume water will flow both in the wick and the channel. Our

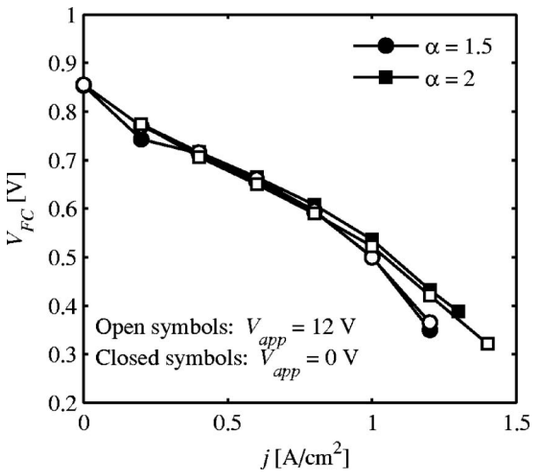

Figure 9. Polarization curves for a porous carbon flow field with 33 0.75 × 0.75 mm channels with and without EO pumping at 12 V. The porous carbon plate shows no signs of flooding when the EO pump is off for these wick dimensions. The MEA for this study was supplied by BCS Fuel Cells (TX) and featured a Nafion 111 membrane, 1.0 mg Pt/cm^2, and carbon cloth GDLs.

postulate is supported by ex situ visualizations of combined water/air flow through these flow fields. These visualizations confirm that the majority of the liquid water travels through the porous carbon. Further, the ex situ experiments clearly show water ejecting from the porous carbon wick at the outlet end of the channels.[a]

Our model requires assumptions regarding the relative pressure fields in the wick and the channel. Throughout much of the surface of the wick/channel interface, capillary forces may act to decouple these pressure fields. However, we here assume there are a significant number of sites that are actively wicking (or ejecting) water. These sites are regions of negligible capillary pressure where local wick pressure is nearly equal to local channel pressure. Thus, the pressure differential across the length of the air channel need not be larger than the wick's capillary pressure for water to leave the wick near the outlet. With this assumption, liquid water will travel through the hydrophilic wick according to a pressure field governed by the pressure gradients in the air stream. The latter is justifiable as the air volume flow rate is typically several thousand times larger than the liquid volume flow rate in the system. Figure 10a depicts the pathways of liquid water into, through, and out of the wick. Figure 10b shows a schematic of our model system and parameters. The single-channel model may be interpreted as analyzing the flow in an array of parallel channels where there is ideal flow uniformity from channel to channel.

For laminar flow, the air pressure gradient, dp/dx, along the gas channel is described by

$$\frac{dp_a}{dx} = \frac{2C\mu_a U_a}{D_h^2} \qquad [2]$$

where C is the geometry-dependent constant associated with the friction factor, $f = C/Re$ ($C = 14.2$ for our aspect ratio rectangle), U_a is the bulk air velocity, μ_a is the viscosity, and D_h is the hydraulic diameter. The air velocity in turn depends on channel geometry, current density, j, and air stoichiometry, α, as follows

[a] Ex situ visualizations were performed with the porous carbon plate featuring 33 0.75 × 0.75 mm channels. Fuel cell operation was simulated by introducing a mixture of vapor-saturated air and liquid water to the inlet of the flow field plate. The water and air flow rates were commensurate with operation at 1 A/cm^2 with an oxygen stoichiometry of 1.5. A video of the visualization is available at http://microfluidics.stanford.edu/litster-JES-2007.htm

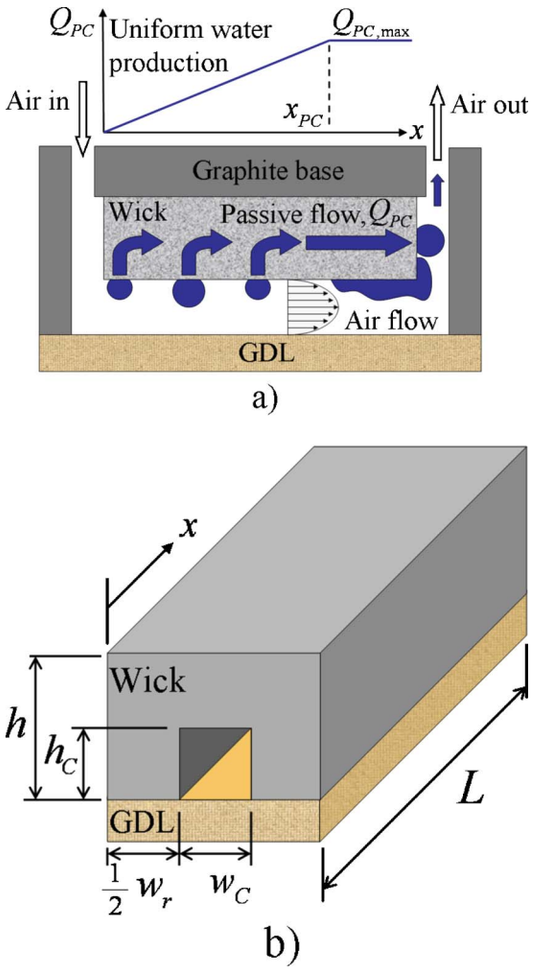

Figure 10. (Color online) Schematic illustration of the transport of liquid water through a passive, hybrid channel/wick system (a), and an idealized geometry for a mathematical model for parallel wick/channel flow driven by the air pressure gradients in the channel (b).

$$U_a = \frac{w_c + w_r}{w_c h_c}\left(1 + \frac{p_{sat}(T)}{p - p_{sat}(T)}\right)\left(\frac{\alpha M_a}{0.21\rho_a}\frac{Lj}{4F}\right) \qquad [3]$$

where w_c and h_c are the width and height of the channel, w_r is the width of the rib, L is the channel length, p and $p_{sat}(T)$ are the static and saturation pressures, and M_a and ρ_a are the air's molecular mass and density. The Darcy equation models the maximum water flow rate in the porous carbon wick that the air pressure gradient can support

$$Q_{PC,max} = (w_c h + w_r h - w_c h_c)\frac{k_{PC}}{\mu_w}\frac{dp_a}{dx} \qquad [4]$$

where k_{PC} is the hydraulic permeability of the porous carbon wick. Assuming a gas stream inlet with 100% inlet relative humidity, the local production of water can be integrated along the channel to yield the total local flow rate of liquid water

$$Q(x) = \frac{M_w}{\rho_w}\frac{(w_c + w_r)j}{2F}x \qquad [5]$$

If the hydraulic resistance of the porous carbon wick is too high, the Darcy flow alone cannot support the water produced. Beyond the point where the product water flow rate meets the capacity of the wick (as determined by the pressure gradient of the air stream), some portion of product water must travel through the channels. The

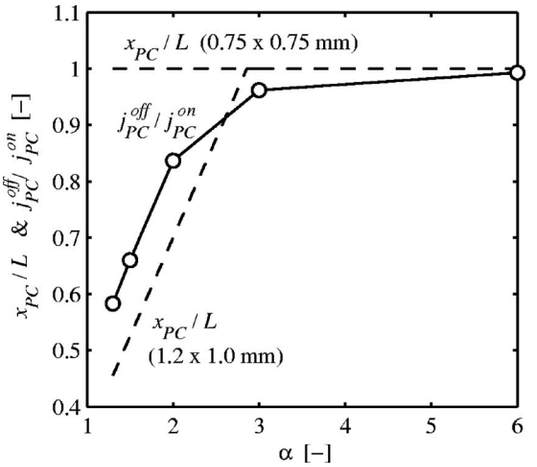

Figure 11. The interpolated fuel cell current from measurements at V_{FC} = 0.6 V with no EO pumping normalized by the current with EO pumping for the flow field with 1.2 × 1.0 mm channels. Along with these experimental measurements, the plot shows the curves of x_{PC}/L (from Eq. 6) for 1.2 × 1.0 mm channels and 0.75 × 0.75 mm channels. We assume a wick permeability to water, k_{PC}, of 5×10^{-11} m^2.[52,53]

expression for the point at which water first flows in the air channel, $x = x_{PC}$ (where $Q_{PC} = Q_{PC,max}$), is found by combining Eq. 2-5

$$\frac{x_{PC}}{L} = \frac{4.76 C k_{PC} \alpha}{D_h^2}\left(1 + \frac{p_{sat}(T)}{p - p_{sat}(T)}\right)\left(\frac{w_c h + w_r h}{w_c h_c} - 1\right)\left(\frac{\mu_a}{\mu_w}\frac{M_a}{M_w}\frac{\rho_w}{\rho_a}\right) \quad [6]$$

Downstream of $x = x_{PC}$, liquid water begins to flow through the gas channel and flooding may occur. Equation 6 shows that this critical location is a function of air stoichiometry, the wick and channel geometry, and the permeability of the wick. Interestingly, this critical location is independent of current density, as the air pressure gradient and water production are both proportional to the current density.

Figure 11 plots x_{PC}/L vs α for two fuel cell flow field designs with channel cross sections of 1.2 × 1.0 mm and 0.75 × 0.75 mm, as determined by Eq. 6. Together with these predictions of x_{PC}/L, the plot also shows experimental data for the ratio of fuel cell current without EO pumping to that with EO pumping, j_{PC}^{off}/j_{PC}^{on}, for the 1.2 × 1.0 mm channels. These measurements are the interpolated fuel cell current at V_{FC} = 0.6 V. We here use j_{PC}^{off}/j_{PC}^{on} as an approximate measure of the portion of the fuel cell area not covered by liquid water. This approach of estimating x_{PC}/L is supported by the visualization work of Liu et al.,[15,21] which showed good agreement between these parameters. Currently, we must also estimate one value in using Eq. 6: the permeability of the porous carbon. A permeability of $k_{PC} = 5 \times 10^{-11}$ m^2 provides a fairly good agreement between Eq. 6 and our experimental data. This permeability value is reasonable considering Gostick et al.[52] and Feser et al.[53] experimentally determined a value of 5×10^{-11} m^2 as the in-plane permeability of uncompressed GDLs. The model qualitatively captures the observed trends in flooding as a function of stoichiometric ratio and is consistent with our ex situ visualizations of water transport.[a]

The model predicts that all of the water travels through the wick for the 0.75 × 0.75 mm channels (and so x_{PC}/L is equal to unity for all α), suggesting this geometry develops enough pressure difference to push water out through the wick and passively mitigate flooding. In contrast, the 1.2 × 1.0 mm channels, which have roughly five times less pressure drop, suffer flooding for α less than about three. These predictions are in good agreement with our polarization experiments. For example, the data of Fig. 9 shows EO pumping has no significant effect for the smaller channels and $\alpha > 2$.

This simple flow model has several implications to active and passive water management using wicks. First, the efficacy of passive wick flow decreases at a lower air stoichiometry due to low available pressure. Second, a large wick cross-sectional area and high permeability are necessary for sufficient passive water transport through the wick. However, thick wicks reduce system volumetric power density and add significant ohmic resistance compared to a nonporous plate. Clearly, both passive and active wick strategies have relative advantages and disadvantages. For the design tested here, we conclude that active EO pumping is preferable for robust operation over a wider range of operating conditions and with a suitably high efficiency and volumetric power density.

Conclusion

Achieving proper membrane humidification without liquid water flooding is a consistent challenge facing PEM fuel cell development. Air flow maldistribution and instability due to flooding limit performance and make parallel channels impractical at high power density. We have demonstrated both active and passive water management in a 25 cm^2 PEM fuel cell with a porous carbon flow field structure which also serves as a wick. The cathode's flow field has 23 parallel air channels. We showed that both passive and active water management alleviate flooding and offer increased power density and stability compared to a nonporous flow field. We presented a simple model for the passive transport of water through the porous carbon wick. Our model and experimental data show that passive water management requires a sufficiently high air pressure gradient in the channels to drive liquid water though the wick. The necessary air pressure gradient is achieved with high air stoichiometry ($\alpha > 3$) for 1.2 mm wide channels. For 0.75 mm wide cathode channels, sufficient pressure is achieved at all stoichiometries, but these smaller channels increase the parasitic load associated with air delivery.

We achieve active water management for all flow fields tested and all operating conditions by integrating an EO pump into the system. The EO pump provides sufficient pressure gradient within the wick to remove excess water from the cell. This system effectively decouples oxidant delivery from liquid water removal for robust, stable operation. The EO pump prevents flooding and provides rapid recovery from severe flooding. With EO pumping we were able to operate the 25 cm^2 fuel cell at an air stoichiometry of 1.3 while maintaining a power density of 0.42 W/cm^2. This is 60% greater than the maximum power density achievable with a nonporous flow field under the same conditions. By comparison, a nonporous flow field requires an air stoichiometry of six for similar performance. EO pumps are compact, have no moving parts, and have a low power requirement that scales appropriately with fuel cell size. Using a simple control algorithm (i.e., always on), the EO pump consumes less than 0.5% of the fuel cell power for moderate to high current densities ($j > 0.3$ A/cm^2). The EO pump consumes less than 2% of the fuel cell power at all operating conditions. The parallel channel architecture also greatly reduces the power required for air delivery (e.g., we need ~0.04 of the air pumping power required for a typical three-channel serpentine design).

Ongoing research is focused on evaluating the feasibility of stacking the water management layers of our design, reducing plate thickness, and system design issues such as active pump control and integrated power conditioning for the EO pump. The ability of the wick to improve membrane humidification when supplying dry gases is also being investigated. In addition, we are studying the influence of active water management on the spatial distribution of current density and the flooding and recovery mechanisms using a segmented anode plate.

Acknowledgments

We gratefully acknowledge a Post-Graduate Scholarship from the Natural Science and Engineering Research Council of Canada for S.L. and a Graduate Research Fellowship from the National Science Foundation for C.R.B.

Stanford University assisted in meeting the publication costs of this article.

List of Symbols

C	friction factor constant
D_h	hydraulic diameter, m
f	friction factor
F	Faraday's constant, 96,487 C/mol
h	height, m
j	current density, A/cm^2 or A/m^2
k_{PC}	porous carbon permeability, m^2
L	air channel length, m
M	molecular mass, kg/mol
N	number of air channels
Δp	air pressure differential, kPa
p	static pressure, Pa
p_{sat}	saturation pressure, Pa
P_{air}	air delivery power, W
P_{EO}	EO pump power, W
P_{FC}	fuel cell power, W
Q	flow rate, m^3/s
Re	Reynolds number
R_{FC}	area specific resistance, Ω cm^2
R_h	hydraulic resistance, Pa s/m^3
t	time, min, s
T	temperature, K
U_a	bulk air velocity, m/s
V_{app}	EO pump applied voltage, V
V_{FC}	fuel cell voltage, V
w	width, m
x	distance, m

Greek

α	air stoichiometry
χ	increase in fuel cell power
η	thermodynamic efficiency
μ	viscosity, Pa s
ρ	density, kg/m^3

Subscripts

a	air
c	channel
PC	porous carbon
r	rib
sat	saturated
w	liquid water

Superscripts

SG	solid graphite
EO,on	porous carbon with EO pumping
EO,off	porous carbon with no EO pumping

References

1. A. Bazylak, D. Sinton, Z. S. Liu, and N. Djilali, *J. Power Sources*, **163**, 784 (2007).
2. J. T. Gostick, M. W. Fowler, M. A. Ioannidis, M. D. Pritzker, Y. M. Volfkovich, and A. Sakars, *J. Power Sources*, **156**, 375 (2006).
3. S. Litster, A. Bazylak, D. Sinton, and N. Djilali, *ECS Trans.*, **3**(1), 409 (2006).
4. S. Litster, D. Sinton, and N. Djilali, *J. Power Sources*, **154**, 95 (2006).
5. P. K. Sinha, P. Halleck, and C.-Y. Wang, *Electrochem. Solid-State Lett.*, **9**, A344 (2006).
6. J. Zhang, D. Kramer, R. Shimoi, Y. Ono, E. Lehmann, A. Wokaun, K. Shinohara, and G. G. Scherer, *Electrochim. Acta*, **51**, 2715 (2006).
7. F.-B. Weng, A. Su, C.-Y. Hsu, and C.-Y. Lee, *J. Power Sources*, **157**, 674 (2006).
8. K. Tuber, D. Pocza, and C. Hebling, *J. Power Sources*, **124**, 403 (2003).
9. T. A. Trabold, J. P. Owejan, D. L. Jacobson, M. Arif, and P. R. Huffman, *Int. J. Heat Mass Transfer*, **49**, 4712 (2006).
10. A. Theodorakakos, T. Ous, M. Gavaises, J. M. Nouri, N. Nikolopoulos, and H. Yanagihara, *J. Colloid Interface Sci.*, **300**, 673 (2006).
11. R. Satija, D. L. Jacobson, M. Arif, and S. A. Werner, *J. Power Sources*, **129**, 238 (2004).
12. N. Pekula, K. Heller, P. A. Chuang, A. Turhan, M. M. Mench, J. S. Brenizer, and K. Unlu, *Nucl. Instrum. Methods Phys. Res. A*, **542**, 134 (2005).
13. J. P. Owejan, T. A. Trabold, D. L. Jacobson, D. R. Baker, D. S. Hussey, and M. Arif, *Int. J. Heat Mass Transfer*, **49**, 4721 (2006).
14. H. P. Ma, H. M. Zhang, J. Hu, Y. H. Cai, and B. L. Yi, *J. Power Sources*, **162**, 469 (2006).
15. X. Liu, H. Guo, and C. Ma, *J. Power Sources*, **156**, 267 (2006).
16. X. Li, I. Sabir, and J. Park, *J. Power Sources*, **163**, 933 (2007).
17. D. Kramer, J. B. Zhang, R. Shimoi, E. Lehmann, A. Wokaun, K. Shinohara, and G. G. Scherer, *Electrochim. Acta*, **50**, 2603 (2005).
18. J. J. Kowal, A. Turhan, K. Heller, J. Brenizer, and M. M. Mench, *J. Electrochem. Soc.*, **153**, A1971 (2006).
19. A. Hakenjos, H. Muenter, U. Wittstadt, and C. Hebling, *J. Power Sources*, **131**, 213 (2004).
20. F. Barbir, H. Gorgun, and X. Wang, *J. Power Sources*, **141**, 96 (2005).
21. X. Liu, H. Guo, F. Ye, and C. F. Ma, *Electrochim. Acta*, **52**, 11 (2007).
22. Q. Yan, H. Toghiani, and H. Causey, *J. Power Sources*, **161**, 492 (2006).
23. R. S. Gemmen and C. D. Johnson, *J. Power Sources*, **159**, 646 (2006).
24. D. Xue and Z. Dong, *J. Power Sources*, **76**, 69 (1998).
25. D. J. Laser and J. G. Santiago, *J. Micromech. Microeng.*, **14**, R35 (2004).
26. D. Kim, C. Buie, and J. G. G. Santiago, *ECS Trans.*, **3**(1), 1181 (2006).
27. W. R. Mérida, G. McLean, and N. Djilali, *J. Power Sources*, **102**, 178 (2001).
28. V. V. Nikam and R. G. Reddy, *Int. J. Hydrogen Energy*, **31**, 1863 (2006).
29. T. V. Nguyen, *J. Electrochem. Soc.*, **143**, L103 (1996).
30. F. Y. Zhang, X. G. Yang, and C. Y. Wang, *J. Electrochem. Soc.*, **153**, A225 (2006).
31. M. A. Hickner, N. P. Siegel, K. S. Chen, D. N. McBrayer, D. S. Hussey, D. L. Jacobson, and M. Arif, *J. Electrochem. Soc.*, **153**, A902 (2006).
32. S. H. Ge, X. G. Li, and I. M. Hsing, *J. Electrochem. Soc.*, **151**, B523 (2004).
33. S. H. Ge, X. G. Li, and I. M. Hsing, *Electrochim. Acta*, **50**, 1909 (2005).
34. K. Sugiura, M. Nakata, T. Yodo, Y. Nishiguchi, M. Yamauchi, and Y. Itoh, *J. Power Sources*, **145**, 526 (2005).
35. M. Watanabe, Y. Satoh, and C. Shimura, *J. Electrochem. Soc.*, **140**, 3190 (1993).
36. J. S. Yi, J. D. L. Yang, and C. King, *AIChE J.*, **50**, 2594 (2004).
37. C. R. Buie, J. D. Posner, T. Fabian, S.-W. Cha, D. Kim, F. B. Prinz, J. K. Eaton, and J. G. Santiago, *J. Power Sources*, **161**, 191 (2006).
38. D. Kim, J. D. Posner, and J. G. Santiago, *Sens. Actuators B*, In press.
39. S. H. Yao and J. G. Santiago, *J. Colloid Interface Sci.*, **268**, 133 (2003).
40. S. H. Yao, D. E. Hertzog, S. L. Zeng, J. C. Mikkelsen, and J. G. Santiago, *J. Colloid Interface Sci.*, **268**, 143 (2003).
41. F. N. Buchi and G. G. Scherer, *J. Electroanal. Chem.*, **404**, 37 (1996).
42. K. R. Cooper and M. Smith, *J. Power Sources*, **160**, 1088 (2006).
43. T. Mennola, M. Mikkola, M. Noponen, T. Hottinen, and P. Lund, *J. Power Sources*, **112**, 261 (2002).
44. R. Zaffou, J. S. Yi, H. R. Kunz, and J. M. Fenton, *Electrochem. Solid-State Lett.*, **9**, A418 (2006).
45. X. G. Yang, F. Y. Zhang, A. L. Lubawy, and C. Y. Wang, *Electrochem. Solid-State Lett.*, **7**, A408 (2004).
46. W. S. He, G. Y. Lin, and T. Van Nguyen, *AIChE J.*, **49**, 3221 (2003).
47. Q. Dong, J. Kull, and M. M. Mench, *J. Power Sources*, **139**, 106 (2005).
48. S. Kim, S. Shimpalee, and J. W. Van Zee, *J. Power Sources*, **135**, 110 (2004).
49. Y. Sone, P. Ekdunge, and D. Simonsson, *J. Electrochem. Soc.*, **143**, 1254 (1996).
50. A. Pozio, R. F. Silva, M. De Francesco, and L. Giorgi, *Electrochim. Acta*, **48**, 1543 (2003).
51. S. Shimpalee, S. Greenway, and J. W. Van Zee, *J. Power Sources*, **160**, 398 (2006).
52. J. T. Gostick, M. W. Fowler, M. D. Pritzker, M. A. Ioannidis, and L. M. Behra, *J. Power Sources*, **162**, 228 (2006).
53. J. P. Feser, A. K. Prasad, and S. G. Advani, *J. Power Sources*, **162**, 1226 (2006).